Civil Engineering Infrastructures Journal, 50(2): 255 – 275, December 2017
Print ISSN: 2322-2093; Online ISSN: 2423-6691
DOI: 10.7508/ceij.2017.02.004

A Hybrid Stress Plane Element with Strain Field

Rezaiee-Pajand, M.[1*] and Yaghoobi, M.[2]

[1] Professor, Ferdowsi University of Mashhad, Mashhad, Iran.
[2] Ph.D. Student, Ferdowsi University of Mashhad, Mashhad, Iran.

Received: 21 Oct. 2016; Revised: 16 Jul. 2017; Accepted: 18 Jul. 2017

ABSTRACT: In this paper, a plane quadrilateral element with rotational degrees of freedom is developed. Present formulation is based on a hybrid functional with independent boundary displacement and internal optimum strain field. All the optimality constraints, including being rotational invariant, omitting the parasitic shear error and satisfying Fliepa's pure bending test, are considered. Moreover, the static equilibrium equations are satisfied in this scheme. Authors' element has only four nodes and twelve degrees of freedom. For the boundary displacement field, Alman's second-order displacement function is employed. The validities of the proposed element are demonstrated by eleven numerical examples: thick curved beam, thin cantilever beam, Cooke's skew beam, thin curved beam, cantilever beam with distortion parameter, high-order patch test, cantilever beam with five and four irregular mesh, Mc Neal's thin cantilever beam and cantilever shear wall with and without openings. When utilizing the coarse and irregular meshes, numerical tests show the high accuracy, rapid convergence and robustness of the suggested element. Less sensitivity to distortion is another property of the new element.

Keywords: Hybrid Functional, Plane Quadrilateral Element, Rotational Degrees of Freedom, Strain States.

INTRODUCTION

Up to now, various plane elements have been created. Most of them are quadrilateral. In general, utilizing these elements in distorted coarse mesh leads to weak responses. To overcome this defect, Hybrid tactic along with the finite element template were employed for presenting new efficient elements (Felippa, 2006). In these methods, the fields used for boundaries differ from the ones deployed inside the element. It should be added that the continuity constraints are not required to be considered in these formulations. Recently, a discussion on how to set up optimal stress in a hybrid element was suggested (Canhui and Suong, 2014). He used the assumed stress, which is based on the Airy fundamental solutions. Other researchers recently demonstrated the advantages of deriving the stress functions from the Airy formula (Cen et al., 2011a; Madeo et al., 2014).

Finite element template is an algebraic parametric form, which is both flexible and diverse schemes. In this technique, the stiffness matrix is considered to have two parts, which are named the base and high-order portions. The higher-order part includes a large number of parameters. By

* Corresponding author E-mail: mrpajand@yahoo.com

specialization of the template, high-performance elements were achieved (Felippa, 2006). It is worth emphasizing; finding the optimality constraints and optimization of the matrix forms are difficult tasks, and they need proper innovation.

For increasing the accuracy of the element, some researchers deployed Alman's second-order displacement field in hybrid approaches (Cen et al., 2011b; Choo et al., 2006; Choi et al., 2006). In other studies, some investigators tried to improve Alman's boundary field (Huang et al., 2010; Cena et al., 2011; Madeo et al., 2012). By mixing the element, which has the rotational degrees of freedom, with the relevant flexural element, the plane shell elements can be obtained. Based on previously experiences, it is deduced that usage of the rotational degrees of freedom increases the performance of the elements in modeling plane problems (Huang et al., 2010; Madeo et al., 2014).

In this article, by using the hybrid functional, a new efficient quadrilateral element for analyzing the plane problems is presented. Formulation is based on employing strain states in the internal field, satisfying equilibrium condition, using optimal conditions of the rotational invariant and eliminating the parasitic shear errors. Moreover, Allman's quadratic displacement is used for independent boundary displacement of the element. The proposed element has four nodes. Each node has two translational degrees of freedom and a rotational one. Drilling degrees of freedom increase the accuracy of noval element (Zouaria et al., 2016; Rojasa et al., 2016; Xing and Zhou, 2016). To construct a flat shell element, it is well known that a membrane element with drilling degrees of freedom can be combined with a plate bending element. In order to verify the accuracy and efficiency of the new strategy, several famous numerical tests are analyzed, and the responses of good quadrilateral elements, belong to the other researchers, are compared to the suggested one. It should be reminded that some of investigators' good quadrilateral elements have more than four nodes. Applying numerical tests disclose the high accuracy, rapid convergence and robustness of authors' element, even in coarse and irregular meshes. Besides, this study demonstrates the less sensitivity to distortion for the presented element. Moreover, using corotational approach, the suggested element is extendable to large elastic deformations (Rezaiee-Pajand and Yaghoobi, 2014).

INTERNAL FIELD BASED ON STRAIN

Various researches have been conducted to create high-performance elements. To achieve great accuracy in the coarse meshes, it is required to find errors and try to remove them. In this study, the optimality constraints are introduced into suggested formulations. To reach the goal, Taylor expansion of the strain field is expressed around the origin as below:

$$\begin{aligned}
&\varepsilon_x(x,y)=(\varepsilon_x)_\circ+(\varepsilon_{x,x})_\circ x+\\
&(\varepsilon_{x,y})_\circ y+(\varepsilon_{x,xx})_\circ(\frac{x^2}{2})+(\varepsilon_{x,xy})_\circ\\
&(x.y)+(\varepsilon_{x,yy})_\circ(\frac{y^2}{2})+...,\\
&\varepsilon_y(x,y)=(\varepsilon_y)_\circ+(\varepsilon_{y,x})_\circ x+\\
&(\varepsilon_{y,y})_\circ y+(\varepsilon_{y,xx})_\circ(\frac{x^2}{2})+\\
&(\varepsilon_{y,xy})_\circ(xy)+(\varepsilon_{y,yy})_\circ(\frac{y^2}{2})+...,\\
&\gamma_{xy}(x,y)=(\gamma_{xy})_\circ+(\gamma_{xy,x})_\circ x+\\
&(\gamma_{xy,y})_\circ y+(\gamma_{xy,xx})_\circ(\frac{x^2}{2})+\\
&(\gamma_{xy,xy})_\circ(xy)+(\gamma_{xy,yy})_\circ(\frac{y^2}{2})+....
\end{aligned} \tag{1}$$

In these relations, the terms with subscript ◦ are named the strain states. For instance, the magnitude of the axial strain ε_x in the origin is shown by $(\varepsilon_x)_\circ$. Moreover, within the neighborhood of the origin, the rate of changes of the axial strain ε_x in x and y directions are demonstrated by $(\varepsilon_{x,x})_\circ$ and $(\varepsilon_{x,y})_\circ$, respectively. In a similar manner, other coefficients can be defined. To obtain the displacement field related to the strain function of Eq. (1), the strain-displacement relations of the plane problem and the rotation function of the linear geometric problem are deployed (Rezaiee-Pajand and Yaghoobi, 2012, 2013, 2014, 2015).

$$\begin{cases} u_x=(u_x)_\circ+(\varepsilon_x)_\circ x+(\gamma_{xy}/2-r_r)_\circ y+ \\ (\varepsilon_{x,x})_\circ x^2/2+(\varepsilon_{x,y})_\circ xy+ \\ (\gamma_{xy,y}-\varepsilon_{y,x})_\circ y^2/2+... \\ u_y=(u_y)_\circ+(\gamma_{xy}/2+r_r)_\circ x+ \\ (\varepsilon_y)_\circ y+(\gamma_{xy,x}-\varepsilon_{x,y})_\circ x^2/2+ \\ (\varepsilon_{y,x})_\circ xy+(\varepsilon_{y,y})_\circ y^2/2+... \end{cases} \quad (2)$$

By considering relationship, which exists between the strain states and the behavioral characteristics of the elements, the analyst can detect element's error and improve its performance. Note that each strain state is a number which denotes the scale factor of a specific mode in the corresponding strain function. The appropriate strain states are selected based on the identification of the efficient modes in each of elements' strain functions. For this purpose, the optimality constraints are used.

It should be reminded that Felippa's bending test has been presented to specify the optimum template of the plane element (Felippa, 2006). In this test, the ability of the element in modeling the correct flexural deformations is investigated. For this purpose, the ratio of the correct energy to the energy obtained from element's formulation is used. By considering the linear strain states related to the axial strain functions in *x* and *y* direction, this test can be satisfied in strain states. According to strain states' formulation, the optimality constraints of being rotational invariant and the ones which omit the parasitic shear error are satisfied when the field function is complete (Rezaiee-Pajand and Yaghoobi, 2012, 2013). If the coordinate axes rotate, the characteristics of the rotational invariant elements do not change. It should be mentioned that the elements may be placed in structural mesh with different angles. In these cases, being rotational invariant is required for creation of the elements. Rotational invariance is a result of the inclusion of all strain field terms with no algebraic order. For example, rotational mapping of a constant strain state has the following form:

$$\begin{aligned} &(\varepsilon_{x'})_\circ=(\varepsilon_x)_\circ\cos^2\theta+ \\ &(\varepsilon_y)_\circ\sin^2\theta+(\gamma_{xy})_\circ\sin\theta\cos\theta \\ &(\varepsilon_{y'})_\circ=(\varepsilon_x)_\circ\sin^2\theta+ \\ &(\varepsilon_y)_\circ\cos^2\theta-(\gamma_{xy})_\circ\sin\theta\cos\theta \\ &(\gamma_{x'y'})_\circ=2\,((\varepsilon_y)_\circ- \\ &(\varepsilon_x)_\circ)\sin\theta\cos\theta+ \\ &(\gamma_{xy})_\circ(\cos^2\theta-\sin^2\theta) \end{aligned} \quad (3)$$

According to this equation, an element is capable of representing constant strains with respect to any system of the coordinates, only if its formulation takes into account all three cases of the constant strain states.

It is worth emphasizing; the axial strain states in the interpolation polynomial of the shear strain lead to the parasitic shear error. As a result, the created element becomes stiffer. In order to gain knowledge about parasitic shear error, the formulation of the

four-node rectangular element is examined. The interpolation functions of this element consist of an incomplete polynomial which contains neither x^2 nor y^2 terms. The strain gradient notation of these terms is as follows:

$$\begin{cases} u = u_\circ + (\varepsilon_x)_\circ x + \\ (\gamma_{xy}/2 - r_r)_\circ y + (\varepsilon_{x,y})_\circ xy \\ v = v_\circ + (\gamma_{xy}/2 + r_r)_\circ x + \\ (\varepsilon_y)_\circ y + (\varepsilon_{y,x})_\circ xy \end{cases} \quad (4)$$

Based on the strain-deformation relations, the interpolation functions of the element can be written in the following form:

$$\begin{cases} \varepsilon_x(x,y) = (\varepsilon_x)_\circ + (\varepsilon_{x,y})_\circ y \\ \varepsilon_y(x,y) = (\varepsilon_y)_\circ + (\varepsilon_{y,x})_\circ x \\ \gamma_{xy}(x,y) = (\gamma_{xy})_\circ + (\varepsilon_{x,y})_\circ x + (\varepsilon_{y,x})_\circ y \end{cases} \quad (5)$$

By examining the shear strain series, it is noticed that the shear strains are independent of the axial strain. In the shear strain interpolation function, two strain states $(\varepsilon_{x,y})_\circ$ and $(\varepsilon_{y,x})_\circ$ improperly appear. Hence, if the element undergoes flexural deformations, the strain states will be nonzero and will incorrectly represent a portion of the shear strain. It should be added that an element, which has strain field function with a complete degree, does not suffer from the parasitic error. In this work, the internal field of the linear strain is deployed for the suggested element. This element includes 12 strain states. In the plane stress and strain states, the static equilibrium equations of a homogenous elastic element have the coming shape:

$$\begin{cases} \dfrac{\partial \sigma_x(x,y)}{\partial x} + \dfrac{\partial \tau_{xy}(x,y)}{\partial y} + F_x(x,y) = 0 \\ \dfrac{\partial \tau_{xy}(x,y)}{\partial x} + \dfrac{\partial \sigma_y(x,y)}{\partial y} + F_y(x,y) = 0 \end{cases} \quad (6)$$

Element's internal force field in *x* and *y* are denoted by $F_x(x,y)$ and $F_y(x,y)$, respectively. Note that these fields are expressed in Cartesian coordinate system. By utilizing strain-stress relation, Eqs. (6) are written in terms of strain fields, as follows:

$$\begin{cases} (2G+\lambda)\varepsilon_{x,x}(x,y) + \lambda\varepsilon_{y,x}(x,y) + \\ G\gamma_{xy,y}(x,y) + F_x(x,y) = 0 \\ \lambda\varepsilon_{x,y}(x,y) + (2G+\lambda)\varepsilon_{y,y}(x,y) + \\ G\gamma_{xy,x}(x,y) + F_y(x,y) = 0 \end{cases} \quad (7)$$

Additionally, for the plane stress and strain states, λ is equal to $\dfrac{\nu E}{(1+\nu)(1-2\nu)}$ and $\dfrac{\nu E}{(1+\nu)(1-\nu)}$, respectively. Moreover, shear modulus, Poisson's ratio and elasticity modulus are shown by G, ν and E, respectively. By assuming a linear strain field and establishing the corresponding static equilibrium equations, two new relationships can be achieved. With the help of these relations, the stain states $(\gamma_{xy,x})_\circ$ and $(\gamma_{xy,y})_\circ$ are obtained based on other strain states. In other words, using the static equilibrium equations reduces the number of strain states to ten. It should be added that usage of these equations improves the performance of the proposed element.

$$\begin{cases} (\gamma_{xy,y})_\circ = -\dfrac{(2G+\lambda)(\varepsilon_{x,x})_\circ + \lambda(\varepsilon_{y,x})_\circ + F_x(x,y)}{G} \\ (\gamma_{xy,x})_\circ = -\dfrac{\lambda(\varepsilon_{x,y})_\circ + (2G+\lambda)(\varepsilon_{y,y})_\circ + F_y(x,y)}{G} \end{cases} \quad (8)$$

$$\mathbf{q}^T = [(u_x)_\circ \quad (u_y)_\circ \quad (r_r)_\circ \quad (\varepsilon_x)_\circ \quad (\varepsilon_y)_\circ \quad (\gamma_{xy})_\circ \quad (\varepsilon_{x,x})_\circ \quad (\varepsilon_{y,x})_\circ \quad (\varepsilon_{x,y})_\circ \quad (\varepsilon_{y,y})_\circ] \tag{9}$$

The vector of the strain states is shown by $\mathbf{q}$. On the other hand, the rigid body motions, $(u_x)_\circ, (u_y)_\circ$ and $(r_r)_\circ$, do not produce strain in the element. Hence, the internal strain field of the element can be written as follows:

$$\varepsilon = \mathbf{B}_q . \bar{\mathbf{q}} \tag{10}$$

$$\mathbf{B}_q = \begin{bmatrix} 1 & 0 & 0 & x & 0 & y & 0 \\ 0 & 1 & 0 & 0 & x & 0 & y \\ 0 & 0 & 1 & -\frac{(2G+\lambda)}{G}y & -\frac{\lambda}{G}y & -\frac{\lambda}{G}x & -\frac{(2G+\lambda)}{G}x \end{bmatrix} \tag{11}$$

$$\bar{\mathbf{q}}^T = \left[(\varepsilon_x)_\circ \quad (\varepsilon_y)_\circ \quad (\gamma_{xy})_\circ \quad (\varepsilon_{x,x})_\circ \quad (\varepsilon_{y,x})_\circ \quad (\varepsilon_{x,y})_\circ \quad (\varepsilon_{y,y})_\circ\right] \tag{10}$$

The modified vector of the strain states is demonstrated by $\bar{\mathbf{q}}$. Note the rigid body motions are omitted from this vector. Furthermore, the internal body forces of the element are assumed to be zero.

BOUNDARY DISPLACEMENT FIELD

The suggested quadrilateral element is named HSSQ, in which, H is the abbreviation of hybrid functional, SS is stand for the strain state, and Q shows the quadrilateral element. This element has four nodes and 12 degrees of freedom. According to Figure 1, each node has two translational degrees of freedom and a rotational one.

To construct the boundary displacement field, Allman's second-order displacements are employed. In the local coordinate system, the aforesaid field for element side ij has the next form:

$$\begin{Bmatrix} \tilde{u}_n \\ \tilde{u}_t \end{Bmatrix} = \begin{bmatrix} \tilde{N}_1 & 0 & -0.5\, l_{ij}\, \tilde{N}_1\, \tilde{N}_2 & \tilde{N}_2 & 0 & 0.5\, l_{ij}\, \tilde{N}_1\, \tilde{N}_2 \\ 0 & \tilde{N}_1 & 0 & 0 & \tilde{N}_2 & 0 \end{bmatrix} \begin{Bmatrix} u_{ni} \\ u_{ti} \\ \omega_i \\ u_{nj} \\ u_{tj} \\ \omega_j \end{Bmatrix} \tag{13}$$

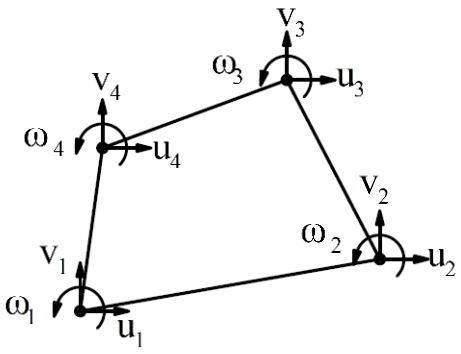

Fig. 1. The geometry of element HSSQ

For side ij, the parameters, which exist in this relation, are shown in Figure 2. The side length is l_{ij}. Also, the displacement fields in n and t directions are shown by $\tilde{u}_n$ and $\tilde{u}_t$, respectively. Furthermore, the rotation of the i-th node is denoted by ω_i. It is worth mentioning; the shape functions are calculated based on the coordinate t, which is shown in Figure 2. On the ij side, the value of this coordinate changes from -1 to 1.

$$\tilde{N}_1=0.5(1-t),\quad \tilde{N}_2=0.5(1+t) \tag{14}$$

In the general coordinates system, Eq. (13) has the subsequent shape:

$$\begin{Bmatrix}\tilde{u}_x\\ \tilde{u}_y\end{Bmatrix}= \begin{bmatrix}\tilde{N}_1 & 0 & -0.5(y_j-y_i)\tilde{N}_1\tilde{N}_2 & \tilde{N}_2 & 0 & 0.5(y_j-y_i)\tilde{N}_1\tilde{N}_2\\ 0 & \tilde{N}_1 & 0.5(x_j-x_i)\tilde{N}_1\tilde{N}_2 & 0 & \tilde{N}_2 & -0.5(x_j-x_i)\tilde{N}_1\tilde{N}_2\end{bmatrix} \begin{Bmatrix}u_{xi}\\ u_{yi}\\ \omega_i\\ u_{xj}\\ u_{yj}\\ \omega_j\end{Bmatrix}=\left[\tilde{N}_{ij}\right]\left\{D_{ij}\right\} \tag{15}$$

FORMULATION OF THE ELEMENT

To find the governing equation of the element, the hybrid stress functional is applied. In this approach, the total energy of the element consists of the internal and boundary energy. The internal energy can be computed by utilizing the succeeding relation:

$$\Pi_C=-0.5\int_V \sigma_{ij}\varepsilon_{ij}dV+\int_{\Gamma_u}\hat{u}_i\sigma_{ij}n_j d\Gamma \tag{16}$$

Furthermore, the interface functional can be calculated by using the next equation:

$$\Pi_d=\int_{\Gamma_i} d_i\sigma_{ij}n_j d\Gamma \tag{17}$$

Γ_u and Γ_i show the boundary of element in internal and interface energy formulas, respectively. As a result, the stress-displacement hybrid functional has the below shape (Rezaiee-Pajand and Karkon, 2014):

$$\Pi_C^d=-0.5\int_V \sigma_{ij}\varepsilon_{ij}dV+\int_{\Gamma} d_i t_i d\Gamma-\int_{\Gamma_t} d_i\hat{t}_i d\Gamma \tag{18}$$

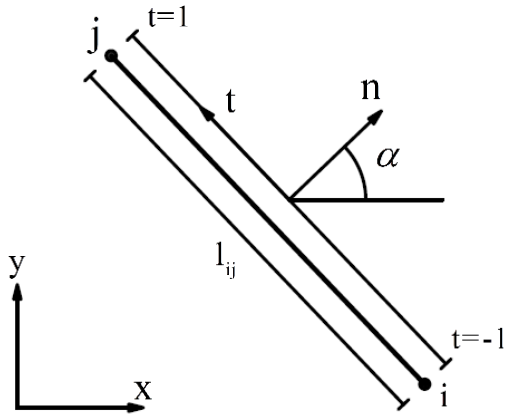

Fig. 2. Characteristics of the boundary displacement field on side ij

where, d_i denotes the assumed boundary displacement field. In the other words, d_i is not defined with $\lim_{x\to\xi} u_i(x)$ if ξ is a boundary point. *u:* is the internal displacement field. Besides, the displacement and boundary stress constraints are shown by $\hat{u}_i$ and $\hat{t}_i$, respectively. In these equations, the internal stress and strain field are shown by σ_{ij} and ε_{ij}, correspondingly. Boundaries of the element and boundary condition with traction are demonstrated by Γ and Γ_t, respectively. By employing the Hook's law, it is intended to set up the relation between stresses and strains. It should be added, the boundary stresses produced by the internal field of the element are shown by t_i. For the suggested element, the following parameters are defined:

$$\varepsilon=\begin{Bmatrix}\varepsilon_x\\ \varepsilon_y\\ \gamma_{xy}\end{Bmatrix}=\mathbf{B}_q.\bar{\mathbf{q}} \tag{19}$$

$$\sigma=\begin{Bmatrix}\sigma_x\\ \sigma_y\\ \tau_{xy}\end{Bmatrix}=$$

$$\begin{bmatrix}2G+\lambda & \lambda & 0\\ \lambda & 2G+\lambda & 0\\ 0 & 0 & G\end{bmatrix}\begin{Bmatrix}\varepsilon_x\\ \varepsilon_y\\ \gamma_{xy}\end{Bmatrix}= \tag{20}$$

$$\mathbf{E}.\varepsilon=\mathbf{E}.\mathbf{B}_q.\bar{\mathbf{q}}$$

$$\mathbf{t}=$$

$$\begin{Bmatrix}T_x\\ T_y\end{Bmatrix}=\begin{bmatrix}n_x & 0 & n_y\\ 0 & n_y & n_x\end{bmatrix}\begin{Bmatrix}\sigma_x\\ \sigma_y\\ \tau_{xy}\end{Bmatrix}= \tag{21}$$

$$\mathbf{A}.\sigma=\mathbf{A}.\mathbf{E}.\mathbf{B}_q.\bar{\mathbf{q}}$$

$$n_x=\cos\alpha=\frac{y_j-y_i}{l_{ij}} \tag{22}$$

$$n_y=\sin\alpha=-\frac{x_j-x_i}{l_{ij}} \tag{23}$$

where, $\mathbf{t}$, n_x and n_y are introduced for the side ij. In addition, the coordinates of the i-th element are denoted by x_i and y_i. In a similar manner, the coordinates of the j-th node are shown by x_j and y_j.

$$\hat{\mathbf{t}}=\begin{Bmatrix}\hat{T}_x\\ \hat{T}_y\end{Bmatrix} \tag{24}$$

$$\hat{\mathbf{u}}=\begin{Bmatrix}\hat{u}_x\\ \hat{u}_y\end{Bmatrix} \tag{25}$$

$$\mathbf{d}_{ij}=\begin{Bmatrix}\tilde{u}_x\\ \tilde{u}_y\end{Bmatrix}_{ij}=\left[\tilde{N}_{ij}\right]\{D_{ij}\} \tag{26}$$

By utilizing these equations, Eq. (18) can be rewritten in the following form:

$$\Pi_C^d=$$
$$-0.5\bar{\mathbf{q}}^T\left(\int_V \mathbf{B}_q^T\mathbf{E}\mathbf{B}_q\,dV\right)\bar{\mathbf{q}}+$$
$$\bar{\mathbf{q}}^T t\left(\int_\Gamma \mathbf{B}_q^T\mathbf{E}\mathbf{A}^T\mathbf{N}\,d\Gamma\right)\mathbf{D}-t\left(\int_{\Gamma_t}\hat{\mathbf{t}}^T\mathbf{N}\,d\Gamma\right)\mathbf{D} \tag{27}$$

in which, *t* denotes the thickness. The entries of the vector denoted by **D** are the element nodal displacements. This vector has the coming shape:

$$\mathbf{D}^{T}=\begin{bmatrix}u_1 & v_1 & \omega_1 & u_2 & v_2 & \omega_2 & u_3 & v_3 & \omega_3 & u_4 & v_4 & \omega_4\end{bmatrix} \tag{28}$$

in the next line, the stress-displacement hybrid functional is minimized with respect to element's strain states vector:

$$\frac{\partial \Pi_C^d}{\partial \bar{\mathbf{q}}} = -\left(\int_V \mathbf{B}_q^T \mathbf{E}\mathbf{B}_q \, dV\right)\bar{\mathbf{q}} + \left(t\int_\Gamma \mathbf{B}_q^T \mathbf{E}\mathbf{A}^T \mathbf{N}\, d\Gamma\right)\mathbf{D} = 0 \tag{29}$$

By employing Eq. (29), the strain state vector can be written based on the nodal displacement vector in the following shape:

$$\bar{\mathbf{q}} = \left(\int_V \mathbf{B}_q^T \mathbf{E}\mathbf{B}_q \, dV\right)^{-1} \left(t\int_\Gamma \mathbf{B}_q^T \mathbf{E}\mathbf{A}^T \mathbf{N}\, d\Gamma\right)\mathbf{D} \tag{30}$$

By making Eq. (27) stationary with respect to the nodal displacement vector and substituting Eq. (30) for the vector of strain states, the next results are achieved:

$$\frac{\partial \Pi_C^d}{\partial \mathbf{D}} = \left(t\int_\Gamma \mathbf{B}_q^T \mathbf{E}\mathbf{A}^T \mathbf{N}\, d\Gamma\right)^T \bar{\mathbf{q}} - \left(t\int_{\Gamma_t} \hat{\mathbf{t}}^T \mathbf{N}\, d\Gamma\right)^T = 0 \tag{31}$$

$$\frac{\partial \Pi_C^d}{\partial \mathbf{D}} = \left(t\int_\Gamma \mathbf{B}_q^T \mathbf{E}\mathbf{A}^T \mathbf{N}\, d\Gamma\right)^T \left(\int_V \mathbf{B}_q^T \mathbf{E}\mathbf{B}_q \, dV\right)^{-1} \left(t\int_\Gamma \mathbf{B}_q^T \mathbf{E}\mathbf{A}^T \mathbf{N}\, d\Gamma\right)\mathbf{D} - \left(t\int_{\Gamma_t} \hat{\mathbf{t}}^T \mathbf{N}\, d\Gamma\right)^T = 0 \tag{32}$$

Consequently, the stiffness matrix and the nodal force vector of the suggested element are computed by the next formula:

$$\mathbf{K} = \left(t\int_\Gamma \mathbf{B}_q^T \mathbf{E}\mathbf{A}^T \mathbf{N}\, d\Gamma\right)^T \left(\int_V \mathbf{B}_q^T \mathbf{E}\mathbf{B}_q \, dV\right)^{-1} \left(t\int_\Gamma \mathbf{B}_q^T \mathbf{E}\mathbf{A}^T \mathbf{N}\, d\Gamma\right) \tag{33}$$

$$\mathbf{P} = \left(t\int_{\Gamma_t} \hat{\mathbf{t}}^T \mathbf{N}\, d\Gamma\right)^T \tag{34}$$

$$\mathbf{K}.\mathbf{D} = \mathbf{P} \tag{35}$$

With the help of triangular coordinates, the amount of $\int_V \mathbf{B}_q^T \mathbf{E}\mathbf{B}_q \, dV$ can be calculated analytically. In this article, the integration is performed on the two triangles, which form the related quadrilateral. Then, the sum of these integrals is computed. Moreover, it is required to express the corresponding relations, in terms of s instead of x and y, for calculation of $\int_\Gamma \mathbf{B}_q^T \mathbf{E}\mathbf{A}^T \mathbf{N}\, d\Gamma$.

$$x = x_i + (x_j - x_i)\frac{(t+1)}{2} \tag{36}$$

$$y = y_i + (y_j - y_i)\frac{(t+1)}{2} \tag{37}$$

$$d\Gamma = \frac{l_{ij}}{2} dt \tag{38}$$

$$\int_\Gamma \mathbf{B}_q^T \mathbf{E}\mathbf{A}^T \mathbf{N}\, d\Gamma = \frac{l_{ij}}{2}\int_\Gamma \left(\mathbf{B}_q(t)\right)\mathbf{E}\mathbf{A}^T \mathbf{N}\, dt \tag{39}$$

NUMERICAL SAMPLES

At this stage, several numerical tests are performed to investigate the robustness of the proposed element. For convenient, all the

quantities used in this section are dimensionless and unit consistence. To compare the results, the responses of other researchers' well-known elements are presented. These elements are listed in the following lines:

1. Four-node isoparametric element; Q4 (Wisniewski and Turska, 2009)
2. Element with internal parameters and formulated by the QACM-I; QACM4 (Cen et al., 2007)
3. Stress hybrid element; PS (Cen et al., 2009)
4. Allman's element; ALLMAN (Choo et al., 2006)
5. Membrane element with drilling degrees of freedom; Q4S (Cen et al., 2009)
6. Hybrid Trefftz plane element; HT (Choo et al., 2006)
7. The modified enhanced assumed strain element; MEAS (Choi et al., 2006; Choo et al., 2006)
8. The quadrilateral Hybrid Trefftz element with rotational degrees of freedom; HTD (Choo et al., 2006)
9. HR element with five modes in skew coordinates; HR5-S (Wisniewski and Turska, 2006, 2009)
10. Enhanced assumed displacement gradient element with four modes; EADG4 (Wisniewski and Turska, 2008, 2009)
11. 8-node membrane element based on three different quadrilateral area coordinate methods, QACM-I, -II, and -III; CQAC-Q8 (Long et al., 2010)
12. 8-node element formulated by the quadrilateral area coordinate method; QACM8 (Cen et al., 2007)
13. Conventional 8-node, 9-node and 12-node quadrilateral isoparametric elements; Q8
14. 4-node quadrilateral element with drilling DOFs based on a mixed formulation; HQ4-9β (Madeo et al., 2012).
15. Quadrilateral element based on strain states' formulation with drilling degrees of freedom; SSQ14 (Rezaiee-Pajand and Yaghoobi, 2015)
16. 8-node membrane element based on strain states' formulation with 18 degrees of freedom; SSQ18 (Rezaiee-Pajand and Yaghoobi, 2015)
17. Hybrid stress element with arbitrary curved edges; Hybrid stress elements with dp = 4, dv = 2 (Santos and Moitinho de Almeida, 2014)

Thick Curved Beam

In this test, a thick curved beam shown in Figure 3 is analyzed. This structure is subjected to the shear force with the magnitude of 600. The elasticity modulus, Poisson's ratio and the thickness are 1000, 0 and 1, respectively. To model this element, four elements are deployed.

It is obvious that use of the quadrilateral elements with straight side leads to the errors. This is because the true boundaries are curved. The vertical displacement of Point A is presented in Table 1. The exact vertical displacement of this point is 90.1 (Cen et al., 2007). It is apparent that the responses of the suggested element lead to more accurate results in comparison to other well-known elements. The number of degrees of freedom in analyzing benchmark problems by each element is different. For example, in this numerical test by HSSQ and Q8 elements, the number of degrees of freedom are 30 and 46, respectively. Therefore, HSSQ element used less computational cost, and obtained the more accurate results.

Table 1. The displacement of Point A in the curved beam under the shear force

Elements	PS	QACM4	Q8	QACM8	SSQ14	SSQ18	HSSQ	Exact (Cen et al., 2007)
Deflection	84.58	84.59	88.6	84.1	87.00	86.45	89.61	**90.1**

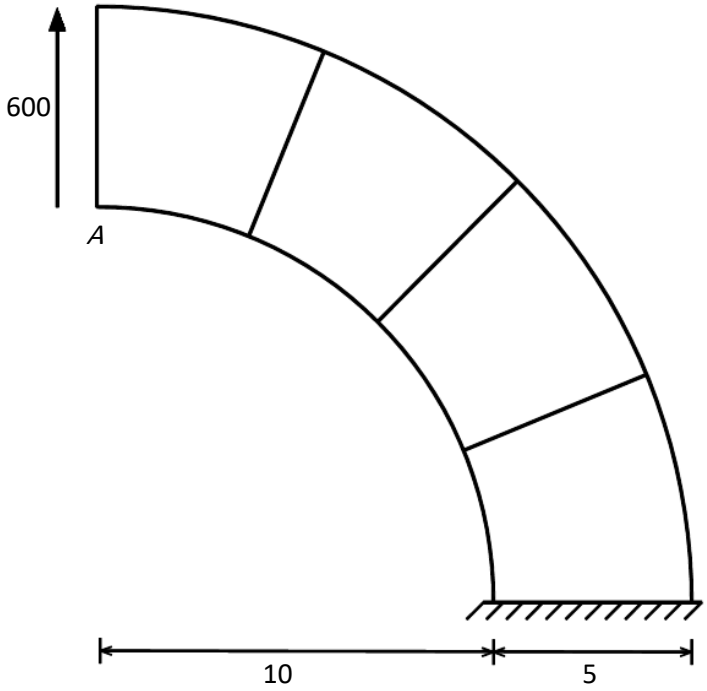

Fig. 3. The geometry and load pattern of the thick curved beam

Thin Cantilever Beam Under In Plane Shear Force

This structure is illustrated in Figure 4. The length, width and thickness of the beam are 100, 1 and 1, respectively. Moreover, the elasticity modulus and Poisson's ratio are 10^6 and 0.3, correspondingly.

Two types, namely 1×100 and 1×200 meshes are deployed to model this structure. In 1×100 mesh, the number of elements used in x and y direction are 100 and 1, respectively. The exact displacements of beam's tip are 3 and 4 (Wisniewski and Turska, 2009). Other researchers' responses are inserted in Table 2. According to these outcomes, element HSSQ leads to the most accurate results. Degrees of freedom for 1×100 and 2×100 meshes for utilizing Q4 element are 404 and 606, respectively. These amounts for HSSQ element are 606 and 909, respectively. Comparing the result of HSSQ element with 1×100 mesh with the response of Q4 element with 2×100 mesh show that HSSQ element, by using equal computational cost, obtained more accurate response.

Table 2. The displacement of the thin cantilever beam's tip under shear force

Elements	Mesh	u_x×100	u_y
Q4	1×100	2.0222	2.6965
	2×100	2.128	2.8371
EADG4, HR5-S	1×100	3	4.0002
	2×100	2.9988	3.9978
SSQ14	1×100	3.000006	4.000242
	2×100	3.193297	4.258160
SSQ18	1×100	2.998288	3.996738
	2×100	2.998900	3.998032
HSSQ	1×100	3.000000	4.000161
	2×100	2.999410	3.998936
Reference value (Wisniewski and Turska, 2009)		**3**	**4**

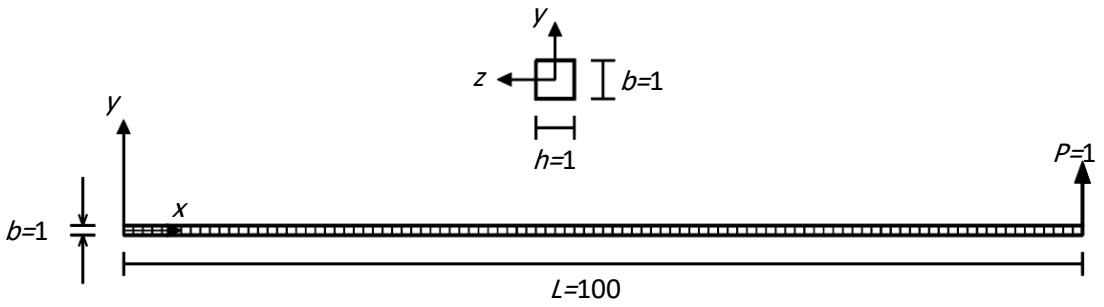

Fig. 4. The geometry of the thin cantilever beam under in plane shear force

Cook's Skew Beam

In general, cook's cantilever trapezoidal beam is analyzed to investigate the robustness of the distorted quadrilateral elements under the shear deformation. The structure is shown in Figure 5. This cantilever beam is subjected to the uniformly distributed shear load of 1 at its end. It should be added that the elasticity modulus, Poisson's ratio and thickness are 1, 1/3 and 1, respectively. Four types meshing, such as, 2×2, 4×4, 8×8 and 16×16 elements are used to analyze cook's cantilever trapezoidal beam.

The obtained vertical displacements of point C are listed in Table 3. Additionally, the maximum stress induced in point A, and also the minimum stress in point B, are demonstrated in Table 4. To compare the outcomes of authors' element, with the other researchers' results, the available solutions are presented, as swell. In this study, answers of the element GT9M8, found for the 64×64 meshes, are considered as the accurate one (Long and Xu, 1994).

Based on Table 3, it is obvious that utilizing the element SSQ18, HTD and HSSQ, with the fine mesh, leads to the most accurate results. Moreover, employing the element HSSQ, with the coarse mesh, produces only 6 percent error in the responses. It is important to note that the element HSSQ gives the more accurate stresses in comparison to the other well-known elements. This property is rooted on the including of the equilibrium equations in authors' formulation. Using proposed element for a 32×32 element mesh, maximum stress in A is 0.2367 and minimum stress at B is -0.2038. Also, the displacement of point C is 23.95. The proposed element, as well as, famous elements of the other researcher converge to the stresses more than the reference solution.

Table 3. The displacement of point C in Cook's beam

Elements	**2×2**	**4×4**	**8×8**	**16×16**
HT	15.04	20.61	22.95	23.68
ALLMAN	21.27	23.06	23.66	23.86
MEAS	21.59	23.06	23.69	23.88
PS	21.13	23.02	-	-
HTD	23.25	23.64	23.83	23.91
QACM4	20.74	22.99	23.69	-
QACM8	22.98	23.74	23.89	-
CQAC-Q8	22.98	23.74	23.89	-
HQ4-9β	22.14	23.37	23.74	23.88
Hybrid stress elements with d_p=4, d_v=2	24.53	24.21	24.16	24.15
SSQ14	27.61	30.48	31.85	32.44
SSQ18	23.45	23.70	23.86	23.92
HSSQ	22.55	23.44	23.79	23.90
Reference value (Long and Xu, 1994)		**23.96**		

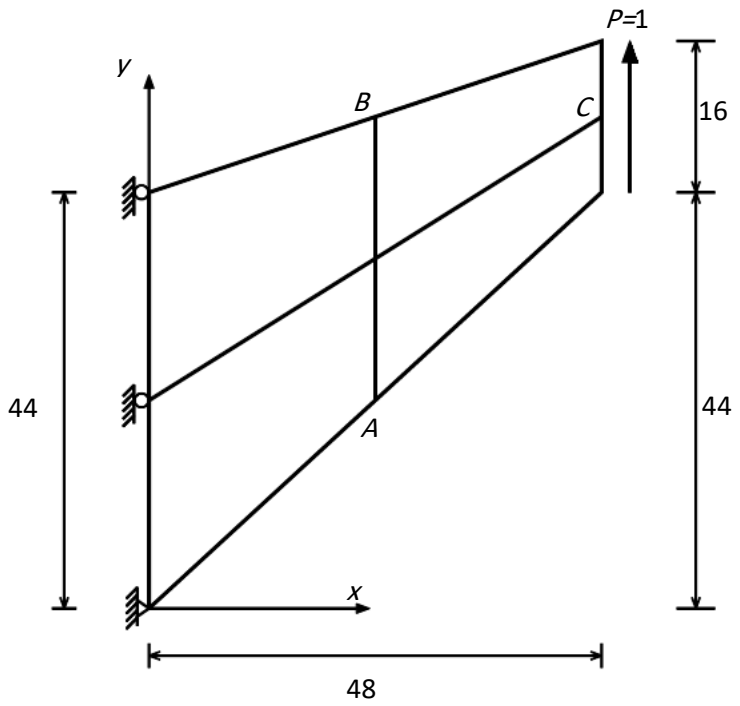

Fig. 5. The geometry and applied load pattern of the Cook's beam

Table 4. The obtained stresses of Cook's beam for 2×2, 4×4, 8×8 and 16×16 meshes

Elements	Maximum Stress at A				Minimum Stress at B			
	2×2	**4×4**	**8×8**	**16×16**	**2×2**	**4×4**	**8×8**	**16×16**
HT	0.1050	0.2020	0.2280	0.2310	-0.2820	-0.2150	-0.1620	-0.1710
ALLMAN	0.1600	0.2360	0.2380	0.2380	-0.2310	-0.1520	-0.1800	-0.1990
MEAS	0.1930	0.2470	0.2450	0.2410	-0.0700	-0.1760	-0.1690	-0.1790
PS	0.1854	0.2241	-	0.2364	-	-	-	-
HTD	0.1720	0.2180	0.2300	0.2350	-0.2310	-0.1880	-0.1930	-0.1980
QACM4	0.1936	0.2256	0.2345	-	-0.1452	-0.1866	-0.1987	-
QACM8	0.1959	0.2414	0.2389	-	-0.2142	-0.2024	-0.2041	-
CQAC-Q8	0.2523	0.2415	0.2389	-	-0.2144	-0.2024	-0.2041	-
HQ4-9β	-	-	-	-	-	-	-	-
Hybrid stress elements with d_p=4, d_v=2	0.2363	0.2352	0.2361	0.2366	0.1887	0.2057	0.2046	0.2038
SSQ14	0.3381	0.2976	0.2864	0.2805	-0.2596	-0.2223	-0.2054	-0.1933
SSQ18	0.2628	0.2360	0.2378	0.2373	-0.2195	-0.2014	-0.2094	-0.2047
HSSQ	0.2158	0.2357	0.2363	0.2367	-0.2085	-0.2029	-0.2026	-0.2039
Reference value (Long and Xu, 1994)	**0.2362**				**-0.2023**			

Thin Curved Beam

In this section, a thin curved beam is analyzed. The related meshes have the aspect ratio of about 5.5. Figure 6 demonstrates the geometry of this structure. This cantilever beam is subjected to shear force of 1 at its free end. Moreover, the elasticity modulus, Poisson's ratio and beam's thickness are 10^7, 0.25 and 0.1, respectively. Note that the exact vertical response of the beam under shear force is 0.08734 (Choo et al., 2006). In Table 5, the vertical displacements of the beam obtained from using other famous elements are listed. According to results, the suggested element leads to the most accurate outcomes in both fine and coarse meshes.

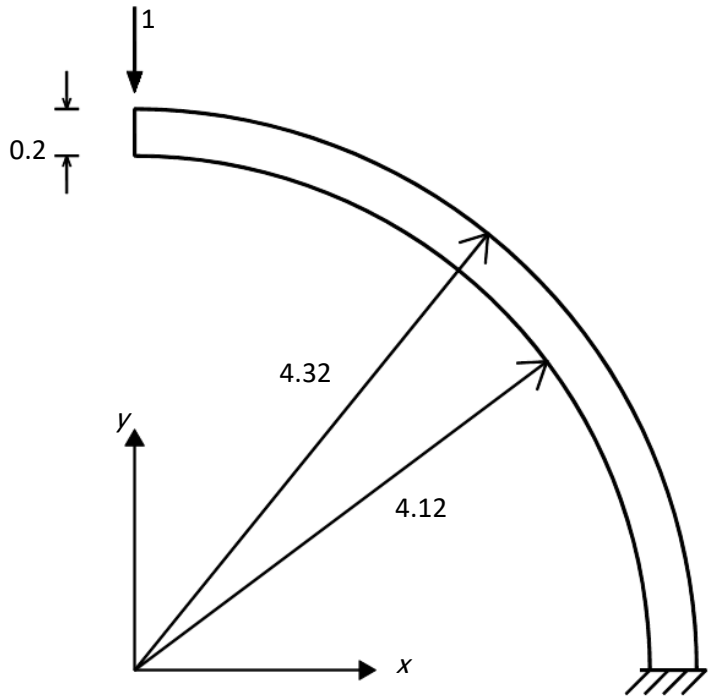

Fig. 6. The geometry of the thin curved beam under shear force at its free end

Table 5. Exact vertical response of the thin curved beam under the shear force

Elements	HT	ALLMAN	MEAS	HTD	Q8	SSQ14	SSQ18	HSSQ	Exact (Fu et al., 2010)
1×6	-0.00662	-0.07756	-0.07756	-0.08420	-0.08759	-0.08748	-0.08745	-0.08797	
2×12	-0.02201	-0.08736	-0.08736	-0.08808	-	-0.08895	-0.08840	-0.08840	**-0.0886**
4×24	-0.04850	-0.08808	-0.08827	-0.08843	-	-0.08925	-0.08850	-0.08851	

Cantilever Beam with Distortion Parameter

A cantilever beam is shown in Figure 7. This structure is modeled by using two elements, the shapes of which vary with the variation of the distorted parameter e. In this test, the aspect ratio is 2.5 for e=0, and the coarse mesh is utilized. Moreover, intensive distortion exists in the deployed meshing. Based on these properties, this test is useful for evaluating the element sensitivity to the distortion. The elasticity modulus, Poisson's ratio and beam's thickness are 0.75, 0.25 and 1, respectively. The applied load pattern is demonstrated in Figure 8. To employ this beam for the bending patch test with linear stress, a moment of the magnitude 1 is applied to structural free end. To perform the bending patch test, the beam should be under shear force of the magnitude 1 at its free end.

For various values of *e*, the responses of the suggested element under different load cases are found and inserted in Tables 6 and 7. The exact displacements of beam's free end under bending moment and shear force are 1 and 6.8333, respectively (Prathap and Senthilkumar, 2008). Based on Table 6, the elements SSQ14, QACM8, HSSQ and SSQ18 are less sensitive to distortion in comparison to other elements. Recall that the number of degrees of freedom for the element HSSQ is less than the other elements. Considering this factor, the sensitivity of the authors' element to the distortion is significantly low. According to the results of Table 7, the use of this element induces 6 percent error in the responses.

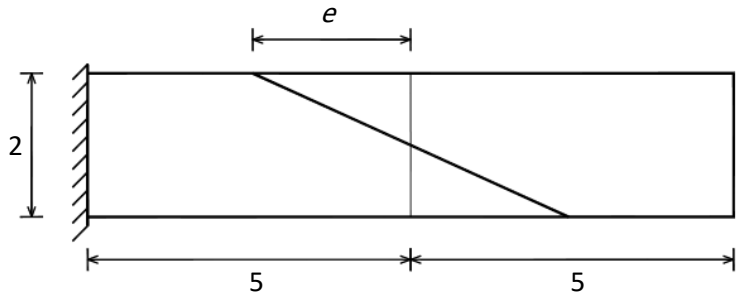

Fig. 7. The geometry of the cantilever beam with distortion parameter *e*

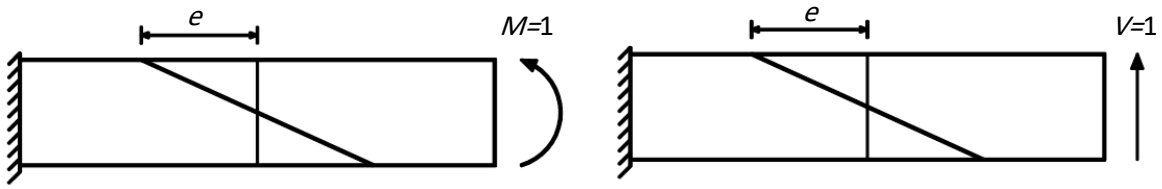

Fig. 8. The load cases for the cantilever beam

Table 6. The normalized displacement of cantilever beam's end under bending moment

e	**0**	**0.5**	**1**	**2**	**3**	**4**
HT	31.5	24.5	17.5	13.6	13.7	14.5
ALLMAN	93.8	95	90.7	56.7	31.8	17.9
MEAS	100	59.5	39.2	30.8	26.9	23.1
PS	100	81	62.9	55	54.7	53.1
HTD	100	99.2	99.6	100.9	83.6	57.8
QACM4	100	83.8	66.5	60.1	61.4	60.3
Q8	100	99.9	99.3	89.39	59.7	32.01
QACM8	100	100	100.2	100.7	101.9	103.7
HQ4-9β	100	99.8	99.1	89.4	68.3	-
SSQ14	99.8	100	100.1	100.7	101.2	102.8
SSQ18	96.6	97.6	98.5	100.4	105.3	116.8
HSSQ	100	100	99.7	98.0	93.6	86.0

Table 7. Normalized displacement of the cantilever beam's end under shear force applied

e	**0**	**1**	**2**	**3**	**4**
Q8	0.9765	0.9298	0.7992	0.5478	0.3255
QACM8	0.9765	0.9483	0.8830	0.8489	0.8421
SSQ14	0.9849	0.9885	0.9948	1.0080	1.0415
SSQ18	0.9466	0.9746	0.9920	1.0293	1.1149
HSSQ	0.9422	0.9687	0.9884	0.9824	0.9458

High-Order Patch Test

In this part, a straight beam is studied. The length and width of the beam are 10 and 1, respectively. As it is shown in Figure 9, this structure is subjected to the pure bending. To analyze the straight beam, regular and distorted meshes are deployed. In each of these meshes, six elements are utilized. The aforementioned meshes are revealed in Figure 9. Furthermore, the elasticity modulus and Poisson's ratio are 100 and 0, respectively. Note that displacements in *x* and *y* directions are denoted by u and v, respectively. The maximum displacements are inserted in Table 8. The exact response to this problem is achieved based on beam theory (Choi et al., 2006). It is worth emphasizing; the use of authors' element, with the distorted meshes, produces only 1 percent error in the responses.

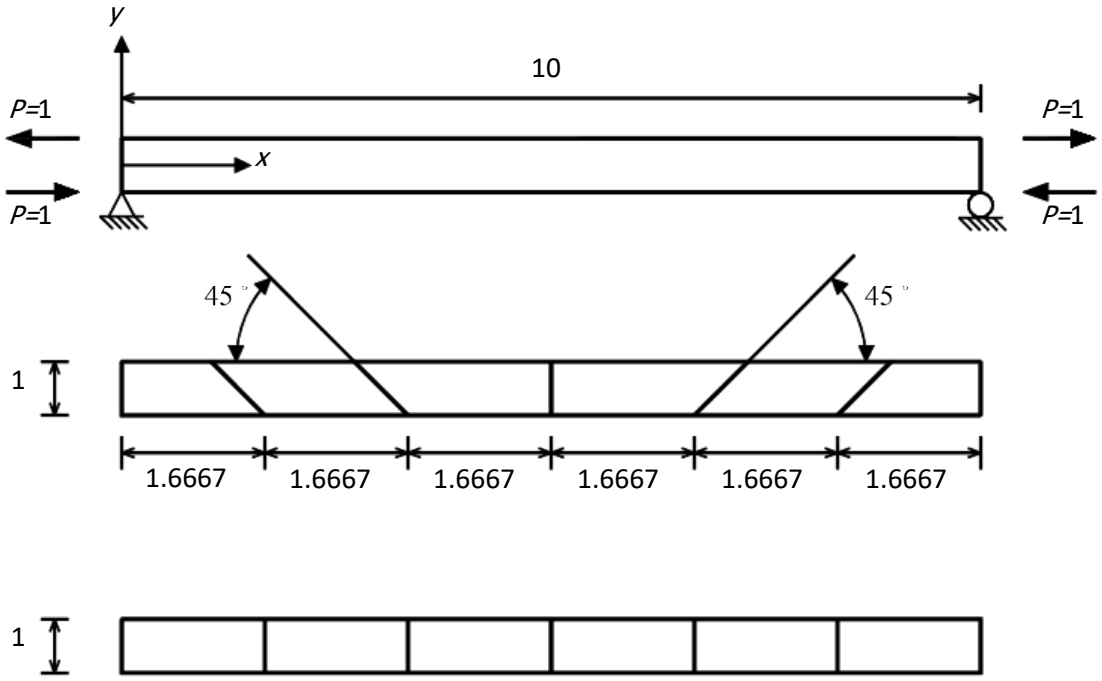

Fig. 9. The load pattern and meshing of the straight beam under pure bending

Table 8. Beam displacements under pure bending

Elements	Regular Mesh		Distorted Mesh	
	Maximum u_x	**Maximum u_y**	**Maximum u_x**	**Maximum u_y**
ALLMAN	-0.6	1.5	-0.498	1.215
HQ4-9β	-	1.5	-	1.51
SSQ14	-0.6	1.5	-0.6	1.5
SSQ18	-0.6	1.5	-0.6	1.5
HSSQ	-0.6	1.5	-0.598	1.516
Exact(Choi et al., 2006)	**-0.6**	**1.5**	**-0.6**	**1.5**

Cantilever Beam with Five Elements and Irregular Mesh

The structural geometry, applied load pattern and the irregular mesh, including five elements, are illustrated in Figure 10. It should be added that the elasticity modulus and Poisson's ratio are 1500 and 0.25, respectively.

The structure is analyzed under two load cases. In the first load pattern, the beam is subjected to the bending moment M. In this case; the structure is under pure bending. In the second load pattern, a concentrated load P is applied to the structure. As a result of this load case, linear bending is produced. Under these two load cases, the exact vertical displacements of the point A are 100.00 and 102.60, respectively (Cen et al., 2009). The responses of other researchers' elements are listed in Table 9. In this table, the responses of various elements are also compared. According to the obtained answers, utilizing the element HSSQ, in the first load case, produces only 0.07 percent error. On the other hand, 1.5 percent error is induced by employing this element when the structure is under the concentrated load P.

Mcneal's Thin Cantilever Beam

There is an important benchmark problem for assessing the sensitivity to the mesh distortion for the quadrilateral elements

(McNeal and Harder, 1985). It is obvious that utilizing the distorted parallelogram and trapezoidal elements with the high aspect ratios reduces the accuracy of results. These issues are investigated in this test. In Figure 11, a thin cantilever beam, with rectangular, trapezoidal and parallelogram meshes, is illustrated. In these meshes, six elements are applied to analyze the structure. Elements' aspect ratio in the meshing with straight side is 5. Furthermore, the elasticity modulus, Poisson's ratio and beam's thickness are 10^7, 0.3 and 0.1, respectively. In this test, the structure is subjected to two load cases. In the first load pattern, a bending moment of magnitude 1 is applied to the beam. In this case, the structure is under pure bending. Moreover, a shear force is applied to the free end of the beam, in the second load case. The exact displacements of the free end under bending and shear load cases are 0.0054 and 0.1081, respectively (Cen et al., 2009).

According to Table 10, the HSSQ element, in both trapezoidal and parallelogram meshes, is insensitive to the distortion under the aforesaid load cases. The outcomes clearly demonstrated that most of other investigators' elements are sensitive to the distortion. In fact, using them in the trapezoidal mesh and under the mentioned loads considerably increases the errors.

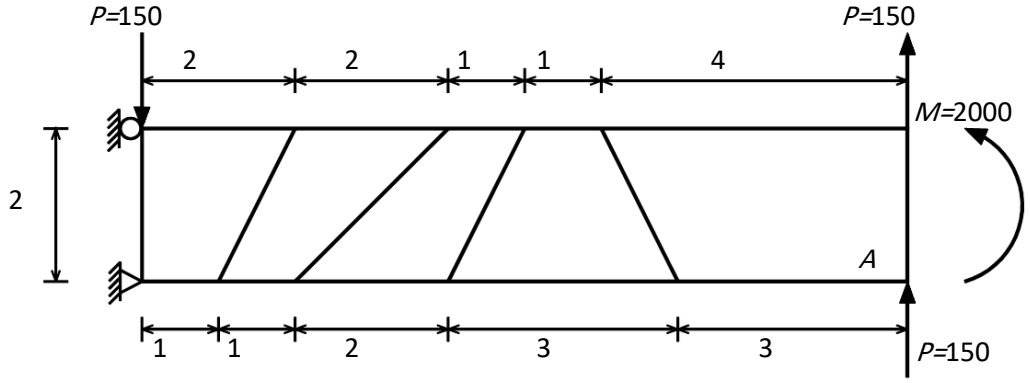

Fig. 10. Cantilever beam with five elements and irregular mesh

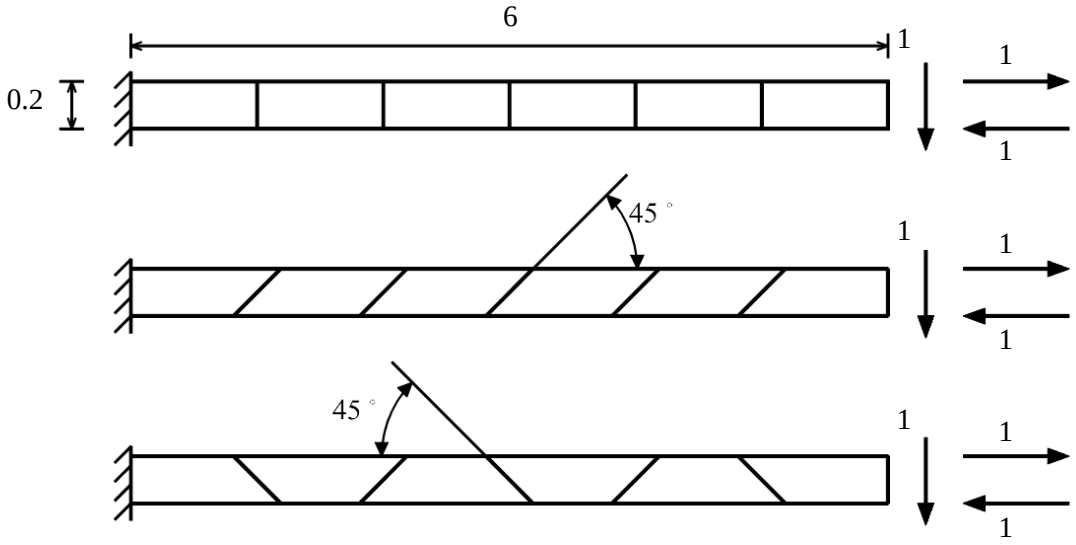

Fig. 11. Rectangular, trapezoidal and parallelogram meshing of McNeal's beam

Table 9. The displacements of the cantilever beam

Elements	M	P
PS	96.18	98.05
QACM4	96.0	98.0
Q8	99.7	101.5
QACM8	101.3	102.8
SSQ14	101.66	104.16
SSQ18	101.48	103.52
HSSQ	99.93	101.01
Exact (Cen et al., 2009)	**100.00**	**102.60**

Table 10. Normalized displacement of the free end of McNeal's beam

Elements	Shear Force at Tip			Bending Moment at Free End		
	Rectangular	Parallelogram	Trapezoidal	Rectangular	Parallelogram	Trapezoidal
ALLMAN	0.904	0.873	0.805	-	-	-
MEAS	0.993	0.621	0.044	-	-	-
PS	0.993	0.798	0.221	1.00	0.852	0.167
QACM4	0.993	0.635	0.052	1.00	0.722	0.046
Q8	0.951	0.919	0.854	1.00	0.994	0.939
QACM8	0.951	0.903	0.895	1.00	1.00	1.00
HQ4-9β	0.992	0.979	0.979	0.999	0.986	0.987
SSQ14	0.983	0.987	0.988	0.989	0.991	0.992
SSQ18	1.00	1.00	1.00	1.00	1.00	1.00
HSSQ	0.993	0.984	0.988	1.00	0.992	0.998

Cantilever Beam with Four Elements and Irregular Mesh

In this test, four irregular quadrilateral elements are used to model the cantilever beam. The geometry of the structure is illustrated in Figure 12. Moreover, the elasticity modulus, Poisson's ratio and beam's thickness are 30000, 0.25 and 1, respectively.

A parabola distributed load is applied to the free end of the beam. The displacements of point A and B are given in Table 11. It is worth emphasizing; the displacements of these points equal to 0.3558 (Cen et al., 2009). By using the current test, the robustness of the proposed element in shear deformations and for irregular meshes is evaluated. According to the obtained answers, usage of the suggested element produces 2 percent error in responses. It is worth emphasizing that comparison to the elements Q8, QACM8, CQAC-Q8, SSQ14 and SSQ18, the element HSSQ has fewer degrees of freedom.

Cantilever Shear Wall without Opening

Herein, the suggested elements are used to analyze a cantilever shear wall which has no opening. In Figure 13, the geometry and applied load of this structure are shown. The elasticity modulus and Poisson's ratio are 2×10^7 and 0.2, respectively. Furthermore, the magnitude of loads P and q are 500 and 100, respectively. This structure is analyzed by using various meshes. These meshes are depicted in Figure 13-2. It should be reminded that the lateral displacement of the highest wall level is computed by utilizing the elements of HSSQ, SSQ18 and Q8. Additionally, various meshes are applied for the calculation of this displacement. Based on Figure 14, the high accuracy of the HSSQ element is proved.

Cantilever Shear Wall with Opening

Figure 15 demonstrates the geometry and applied load of the shear wall with opening. The elasticity modulus and Poisson's ratio of this structure are 2×10^7 and 0.2, respectively. Additionally, the wall thickness is 0.4, and the magnitude of force P is 500.

To analyze this structure, two meshes, namely a and b, are utilized. These meshes are illustrated in Figure 15-2. By employing the presented element and the aforesaid meshes, the lateral displacements of the roof stories, 2, 4, 6 and 8, are computed. Moreover, the responses of the elements HSSQ, SSQ14, SSQ18 and Q8 are calculated for the aforementioned meshes. In Table 12, the obtained answers are listed. For comparison, the responses of the Q8 element in a fine mesh is presented, as well. In this meshing, the wall is divided into 0.1×0.1 square elements. This mesh denoted by c includes 26880 of the Q8 elements.

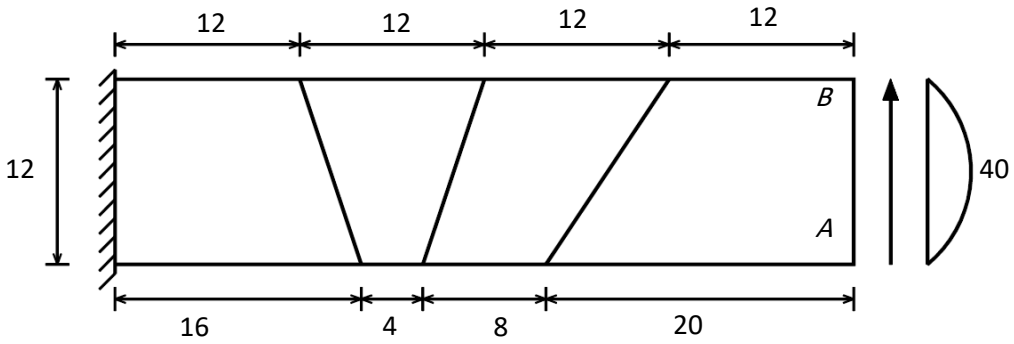

Fig. 12. Cantilever beam with four elements and irregular mesh

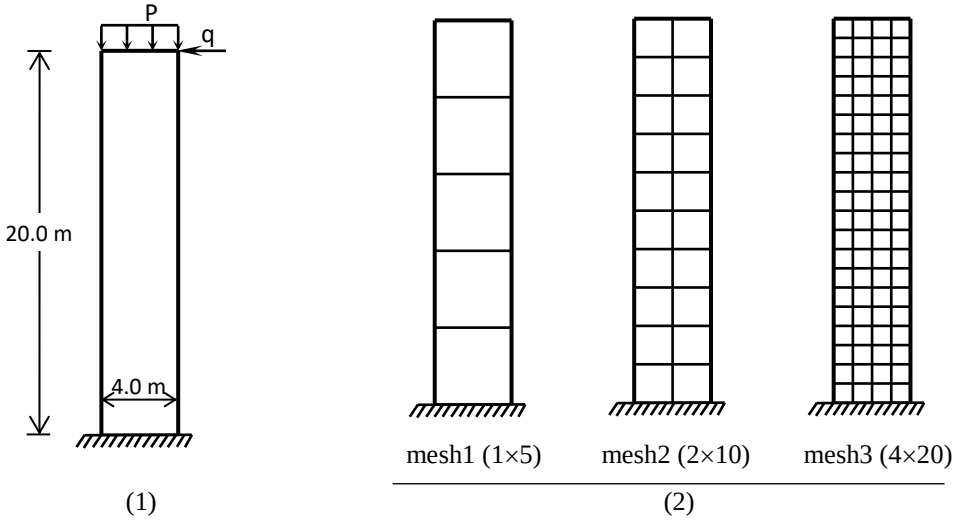

Fig. 13. Geometry, load pattern and meshes of the cantilever shear wall without opening

Table 11. The displacements of the cantilever beam under the parabola shear distributed

Elements	Tip Deflection		
	Point A	Point B	Average
Q4S	-	-	0.2978
QACM4	0.3280	0.3305	0.3293
Q8	0.3481	0.3474	0.3479
QACM8	0.3524	0.3517	0.3520
CQAC-Q8	0.3529	0.3520	0.3524
SSQ14	0.3559	0.3559	0.3559
SSQ18	0.3526	0.3520	0.3523
HSSQ	0.3506	0.3469	0.3488
Exact (Cen et al., 2009)		**0.3558**	

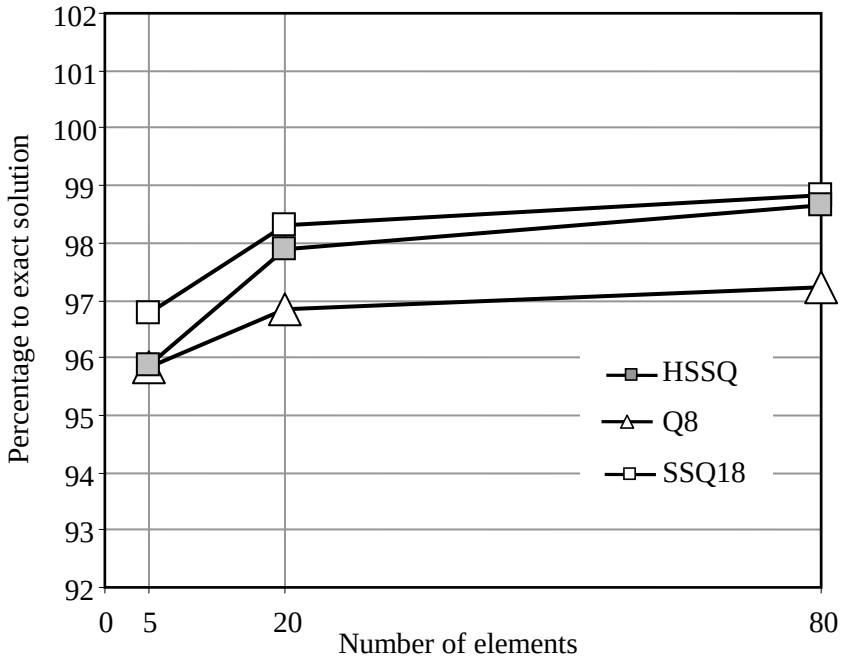

Fig. 14. The normalized lateral displacement at the top of the cantilever shear wall without opening

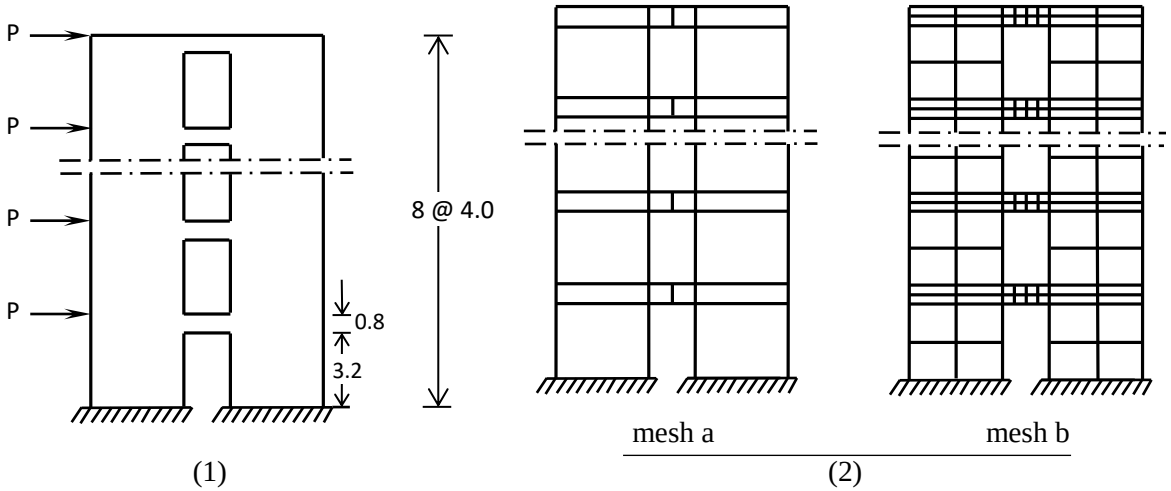

Fig. 15. Geometry, load pattern and meshes of the shear wall with opening

Table 12. The lateral displacements of stories 2, 4, 6 and 8 of the cantilever shear wall with opening

Element	Model	Lateral Displacement at Floor Level			
		Floor 2	Floor 4	Floor 6	Floor 8
Q8	a	0.56	1.53	2.59	3.62
	b	0.68	1.82	3.02	4.16
SSQ14	a	0.90	2.62	4.61	6.63
	b	1.14	3.22	5.49	7.70
SSQ18	a	0.76	2.03	3.36	4.61
	b	0.80	2.13	3.51	4.81
HSSQ	a	0.71	1.91	3.18	4.40
	b	0.79	2.10	3.47	4.75
Q8	**c**	**0.90**	**2.38**	**3.91**	**5.35**

CONCLUSIONS

To present a new plane element, two independent fields were used. They were internal strain function and boundary displacement field. In this formulation, the continuity constraints were not required. The internal strain filed was expressed based on the strain states. For being rotational invariant, a complete strain field was selected. By the help of this technique, the errors, which were rooted in parasitic shear, were eliminated. Based on the results, the suggested element performed well in the Feilipa's pure bending test. It should be added that the static equilibrium equations were satisfied for the internal strain field, as well. Fulfillment of these conditions reduced the number of strain states and increased the robustness of the new element. Besides, Alman's second-order displacement function was deployed for the boundary displacement field. Because authors' element has rotational degrees of freedom, it can be combined with the bending element to produce a good shell element. The high accuracy, rapid convergence, insensitivity to the distortion, in both fine and coarse meshes, are the most important characteristics of authors' formulation. By solving several complex and famous problems, the robustness of new element was completely investigated numerically.

REFERENCES

Canhui, Z. and Suong, V.H. (2014). "A systematic and quantitative method to determine the optimal assumed stress fields for hybrid stress finite elements", *Finite Elements in Analysis and Design*, 80, 41-62.

Cen, S., Chen, X.M. and Fu, X.R. (2007). "Quadrilateral membrane element family formulated by the quadrilateral area coordinate method", *Computer Methods in Applied Mechanics and Engineering*, 196(41-44), 4337-4353.

Cen, S., Chen, X.M., Li, C.F. and Fu, X.R. (2009). "Quadrilateral membrane elements with analytical element stiffness matrices formulated by the new quadrilateral area coordinate method (QACM-II)", *International Journal for Numerical Methods in Engineering*, 77, 1172-1200.

Cen, S., Fu, X.R. and Zhou, M.J. (2011a). "8- and 12-node plane hybrid stress-function elements immune to severely distorted mesh containing elements with concave shapes", *Computer Methods in Applied Mechanics and Engineering*, 200, 2321-2336.

Cen, S., Zhou, M.J. and Fu, X.R. (2011b). "A 4-node hybrid stress-function (HS-F) plane element with drilling degrees of freedom less sensitive to severe mesh distortions", *Computers and Structures*, 89, 517-528.

Cena, S., Zhoua, M.J. and Fub, X.R. (2011). "A 4-node hybrid stress-function (HS-F) plane element with drilling degrees of freedom less sensitive to severe mesh distortions", *Computers and Structures*, 89(5-6), 517-528.

Choi, N., Choo, Y.S. and Lee, B.C. (2006). "A hybrid Trefftz plane elasticity element with drilling degrees of freedom", *Computer Methods in Applied Mechanics and Engineering*, 195, 4095-4105.

Choo, Y.S., Choi, N. and Lee, B.C. (2006). "Quadrilateral and triangular plane elements with rotational degrees of freedom based on the hybrid Trefftz method", *Finite Elements in Analysis and Design*, 42, 1002-1008.

Felippa, C.A. (2006). "Supernatural QUAD4: a template formulation", invited contribution to J.H. Argyris Memorial Issue, *Computer Methods in Applied Mechanics and Engineering*, 195, 5316-5342.

Fu, X.R., Cen, S., Li, C.F. and Chen, X.M. (2010). "Analytical trial function method for development of new 8-node plane element based on the variational principle containing Airy stress function", *Engineering Computations*, 27(4), 442-463.

Huang, M., Zhao, Z. and Shen, C. (2010). "An effective planar triangular element with drilling rotation", *Finite Elements in Analysis and Design*, 46, 1031-1036.

Long, Y.Q. and Xu, Y. (1994). "Generalized conforming quadrilateral membrane element with vertex rigid rotational freedom", *Computers and Structures*, 52(4), 749-755.

Long, Z.F., Cen, S., Wang, L., Fu, X.R. and Long, Y.Q. (2010). "The third form of the quadrilateral area coordinate method (QACM-III): theory, application, and scheme of composite coordinate interpolation", *Finite Elements in Analysis and Design*, 46(10), 805-818.

Madeo, A., Casciaro, R., Zagari, G., Zinno, R. and Zucco, G. (2014). "A mixed isostatic 16 DOF

quadrilateral membrane element with drilling rotations, based on Airy stresses", *Finite Elements in Analysis and Design*, 89, 52-66.

Madeo, A., Zagari, G. and Casciaro, R. (2012). "An isostatic quadrilateral membrane finite element with drilling rotations and no spurious modes", *Finite Elements in Analysis and Design*, 50, 21-32.

McNeal, R.H. and Harder, R.L. (1985). "A proposed standard set of problems to test finite element accuracy", *Finite Elements in Analysis and Design*, 1(1), 3-20.

Prathap, G. and Senthilkumar, V. (2008). "Making sense of the quadrilateral area coordinate membrane elements", *Computer Methods in Applied Mechanics and Engineering*, 197(49-50), 4379-4382.

Rezaiee-Pajand, M. and Karkon, M. (2014). "Hybrid stress and analytical functions for analysis of thin plates bending", *Latin American Journal of Solid and Structures*, 11, 556-579.

Rezaiee-Pajand, M. and Yaghoobi, M. (2012). "Formulating an effective generalized four-sided element", *European Journal of Mechanics A/Solids*, 36, 141-155.

Rezaiee-Pajand, M. and Yaghoobi, M. (2013). "A free of parasitic shear strain formulation for plane element", *Research in Civil and Environmental Engineering*, 1, 1-27.

Rezaiee-Pajand, M. and Yaghoobi, M. (2014). "An efficient formulation for linear and geometric non-linear membrane elements", *Latin American Journal of Solid and Structures*, 11, 1012-1035.

Rezaiee-Pajand, M. and Yaghoobi, M. (2015). "Two new quadrilateral elements based on strain states", *Civil Engineering Infrastructures Journal*, 48(1), 133-156.

Rojasa, F., Andersonb, J.C. and Massonea, L.M. (2016). "A nonlinear quadrilateral layered membrane element with drilling degrees of freedom for the modeling of reinforced concrete walls", *Engineering Structures*, 124, 521-538.

Santos, H.A.F.A. and Moitinho de Almeida, J.P. (2014). "A family of Piola-Kirchhoff hybrid stress finite elements for two-dimensional linear elasticity", *Finite Elements in Analysis and Design*, 85, 33-49.

Wisniewski, K. and Turska, E. (2006). "Enhanced Allman quadrilateral for finite drilling Rotations", *Computer Methods in Applied Mechanics and Engineering*, 195, 6086-6109.

Wisniewski, K. and Turska, E. (2008). "Improved four-node Hellingere Reissner elements based on skew coordinates", *International Journal for Numerical Methods in Engineering*, 76, 798-836.

Wisniewski, K. and Turska, E. (2009). "Improved 4-node Hu-Washizu elements based on skew coordinates", *Computers and Structures*, 87, 407-424.

Xing, C. and Zhou, C. (2016). "A singular planar element with rotational degree of freedom for fracture analysis", *Theoretical and Applied Fracture Mechanics*, 86, 239-249.

Zouaria, W., Hammadib, F. and Ayadc, R. (2016). "Quadrilateral membrane finite elements with rotational DOFs for the analysis of geometrically linear and nonlinear plane problems", *Computers and Structures*, 173, 139-149.